

Atmospheric Rossiter-McLaughlin effect and transmission spectroscopy of WASP-121b with ESPRESSO[★]

F. Borsa¹, R. Allart², N. Casasayas-Barris^{6,7}, H. Tabernero¹⁰, M. R. Zapatero Osorio⁸, S. Cristiani^{5,19}, F. Pepe², R. Rebolo^{6,7,17}, N. C. Santos^{10,11}, V. Adibekyan^{10,11}, V. Bourrier², O. D. S. Demangeon^{10,11}, D. Ehrenreich², E. Pallé^{6,7}, S. Sousa¹⁰, J. Lillo-Box⁸, C. Lovis², G. Micela⁹, M. Oshagh^{6,7}, E. Poretti^{1,4}, A. Sozzetti³, C. Allende Prieto^{6,7}, Y. Alibert¹⁴, M. Amate^{6,7}, W. Benz¹⁴, F. Bouchy², A. Cabral^{15,16}, H. Dekker¹³, V. D’Odorico^{5,19}, P. Di Marcantonio⁵, P. Figueira^{18,10}, R. Genova Santos^{6,7}, J. I. González Hernández^{6,7}, G. Lo Curto¹⁸, A. Manescau¹³, C. J. A. P. Martins^{10,12}, D. Mégevand², A. Mehner¹⁸, P. Molaro^{5,19}, N. Nunes^{15,16}, M. Riva¹, A. Suárez Mascareño^{6,7}, S. Udry², and F. Zerbi¹

(Affiliations can be found after the references)

Received ; accepted

ABSTRACT

Context. Ultra-hot Jupiters are excellent laboratories for the study of exoplanetary atmospheres. WASP-121b is one of the most studied; many recent analyses of its atmosphere report interesting features at different wavelength ranges.

Aims. In this paper we analyze one transit of WASP-121b acquired with the high-resolution spectrograph ESPRESSO at VLT in one-telescope mode, and one partial transit taken during the commissioning of the instrument in four-telescope mode.

Methods. We take advantage of the very high S/N data and of the extreme stability of the spectrograph to investigate the anomalous in-transit radial velocity curve and study the transmission spectrum of the planet. We pay particular attention to the removal of instrumental effects, and stellar and telluric contamination. The transmission spectrum is investigated through single-line absorption and cross-correlation with theoretical model templates.

Results. By analyzing the in-transit radial velocities we were able to infer the presence of the atmospheric Rossiter-McLaughlin effect. We measured the height of the planetary atmospheric layer that correlates with the stellar mask (mainly Fe) to be $1.052 \pm 0.015 R_p$ and we also confirmed the blueshift of the planetary atmosphere. By examining the planetary absorption signal on the stellar cross-correlation functions we confirmed the presence of a temporal variation of its blueshift during transit, which could be investigated spectrum-by-spectrum thanks to the quality of our ESPRESSO data. We detected significant absorption in the transmission spectrum for Na, H, K, Li, Ca II, and Mg, and we certified their planetary nature by using the 2D tomographic technique. Particularly remarkable is the detection of Li, with a line contrast of $\sim 0.2\%$ detected at the 6σ level. With the cross-correlation technique we confirmed the presence of Fe I, Fe II, Cr I, and V I. H α and Ca II are present up to very high altitudes in the atmosphere ($\sim 1.44 R_p$ and $\sim 2 R_p$, respectively), and also extend beyond the transit-equivalent Roche lobe radius of the planet. These layers of the atmosphere have a large line broadening that is not compatible with being caused by the tidally locked rotation of the planet alone, and could arise from vertical winds or high-altitude jets in the evaporating atmosphere.

Key words. planetary systems – techniques: spectroscopic – techniques: radial velocities – planets and satellites: atmospheres – stars: individual: WASP-121

1. Introduction

Ultra-hot Jupiters (UHJs) are giant exoplanets on short-period orbits ($P \leq 3$ days) that receive very intense irradiation from their host stars (equilibrium temperature $T_{eq} \geq 2000$ K). As a consequence, their expanded atmospheres are in extreme states, experiencing phenomena like atmospheric evaporation and escape (e.g., Vidal-Madjar et al. 2003; Fossati et al. 2010; Yan & Henning 2018; Bourrier & des Etangs 2018; Sing et al. 2019). Most of the major molecules (except CO) are thermally dissociated into their atomic constituents in the atmospheres of UHJs (Parmentier et al. 2018; Lothringer et al. 2018). Given their high equilibrium temperatures, iron is also often found in the gaseous

state (e.g., Hoeijmakers et al. 2018; Casasayas-Barris et al. 2019; Ehrenreich et al. 2020; Cabot et al. 2020).

High-resolution transmission spectroscopy is one of the most powerful tools to study exoplanetary atmospheres (e.g., Deming & Seager 2017). While investigating different layers of the planetary atmospheres, it resolves the possible ambiguities present in low-resolution spectra (e.g., molecular identification and abundance determinations when multiple species overlap; Brogi et al. 2017), and it allows us to spectroscopically separate the planetary and stellar restframes (e.g., Snellen et al. 2010; Brogi et al. 2016; Borsa & Zannoni 2018; Casasayas-Barris et al. 2019). Recently, in-transit radial velocities (RVs) also demonstrated their capacity to scan the atmosphere of hot exoplanets. In-transit RVs are affected by a deviation from the Keplerian motion around the star–planet center of mass, known as the Rossiter-McLaughlin effect (RM; Rossiter 1924; McLaughlin 1924), which is caused by the stellar rotation. The shape and amplitude of this deformation depend on the projected spin-orbit angle (e.g., Winn et al. 2008), on $v \sin i$ and the radius of the planet at any given wave-

Send offprint requests to: F. Borsa
e-mail: francesco.borsa@inaf.it

[★] Based in part on Guaranteed Time Observations collected at the European Southern Observatory under ESO programme 1102.C-0744 by the ESPRESSO Consortium.

length (Snellen 2004; Dreizler et al. 2009; Di Gloria et al. 2015). In addition, if the atmosphere of the planet contains elements that are present in the stellar mask used to determine the RVs (e.g., Fe), another deformation is added to the classic RM, whose amplitude is proportional to the height of the atmospheric layers that correlate with the stellar mask (the atmospheric RM; Borsa et al. 2019).

WASP-121b ($M_p \sim 1.2 M_J$, $R_p \sim 1.7 R_J$, Delrez et al. 2016) is one of the most studied transiting UHJs. Orbiting a bright ($V=10.4$ mag) F6 star in ~ 1.27 days and with a misaligned projected spin-orbit angle ($\lambda = 87.2^\circ$, Bourrier et al. 2020), it is an excellent target for atmospheric follow-up investigation. Salz et al. (2019) found excess absorption in near-UV transit observations with the *Swift* satellite, possibly caused by Fe II in a dense extended atmosphere. Fe II was then confirmed in its exosphere with *Hubble Space Telescope* (HST) observations, as was Mg II (Sing et al. 2019). HST also provided an optical transmission (Evans et al. 2018) and optical+infrared emission spectra, which led to the detection of water in emission (Evans et al. 2017) and to an estimation of the metallicity and C/O (Mikal-Evans et al. 2019). A secondary eclipse was also detected with a 1m class telescope at $2\mu\text{m}$ (Kovács & Kovács 2019). Phase curve observations with TESS pointed to a temperature inversion possibly caused by VO and TiO (Bourrier et al. 2020), but there was no evidence of these compounds at the terminator (Merritt et al. 2020). With high-resolution UVES transit observations, Gibson et al. (2020) detected Fe I low in the atmosphere. Using HARPS transit observations, Bourrier et al. (2020) again found evidence for the presence of iron in the atmosphere by discovering that it correlates with the stellar mask used to extract the cross-correlation functions (CCFs). With the same dataset Cabot et al. (2020) detected Na I, H α , and again Fe I, and Ben-Yami et al. (2020) also found evidence of the presence of Cr I and V I.

In this manuscript we present the analysis of high-resolution spectroscopic transit observations of WASP-121b with the Echelle Spectrograph for Rocky Exoplanets and Stable Spectroscopic Observations (ESPRESSO; Pepe et al. 2010, 2014, 2020). We first present the observations (Sect. 2). Then we perform a stellar characterization (Sect. 3), followed by an analysis of the in-transit RVs and of the planetary atmospheric signal imprinted in the stellar cross-correlation functions (Sect. 4). We then present the analysis of the planetary transmission spectrum (Sect. 5), and finally discuss our results (Sect. 6).

2. Data sample

We analyze two transits of WASP-121b observed with ESPRESSO. ESPRESSO is a fiber-fed, ultra-stabilized echelle high-resolution spectrograph, with the capability of collecting light from each 8.2m Unit Telescope (UT) of the Very Large Telescope (VLT) individually or the four UTs simultaneously, yielding a 16m-equivalent telescope. It is the first instrument with this capability, and it is located in the VLT Combined-Coudé Laboratory. ESPRESSO covers the optical wavelength range 3800-7880 Å.

One transit of WASP-121b was observed as part of the Guaranteed Time Observation in 1-UT HR21 mode (resolving power $R \sim 138,000$) under program 1102.C-0744, using UT3 Melipal. We also analyze one partial transit of WASP-121b observed in 4-UT MR42 mode ($R \sim 70,000$) during the commissioning of the instrument. Despite the lower resolution with respect to the HR mode, the 4-UT MR spectra benefit from the higher signal-to-noise ratio (S/N). Observing conditions were good and compa-

table during the two transits, with an average seeing of ~ 0.8 . A log of the observations is presented in Table 1.

For the 1-UT transit, while fiber A of the instrument was observing the target, fiber B was pointing to the sky. Instead, for the 4-UT transit fiber B was put on the Fabry-Perot simultaneous reference. We analyzed the 1D spectra extracted by the Data Reduction Software (DRS) pipeline¹. In the case of the 1-UT transit, we analyzed the sky-subtracted 1D spectra.

3. Stellar characterization

We calculated the stellar parameters of WASP-121 by means of a spectral synthesis analysis on a combined spectrum of the 1-UT night using the SteParSyn code (Tabernero et al. 2018). It uses a Markov chain Monte Carlo process to derive the probability distribution functions of the stellar atmospheric parameters through a grid of synthetic spectra, using MARCS models (Gustafsson et al. 2008) and the Fe I-Fe II line list for metal-rich dwarf stars described in Tabernero et al. (2019). The derived T_{eff} , $\log g$, and metallicity (Table 2) are in agreement with the values of Delrez et al. (2016), while the $v \sin i$ value calculated with line broadening is slightly lower than theirs (11.8 ± 0.2 versus $13.5 \pm 0.7 \text{ km s}^{-1}$). Using the Padova stellar model isochrones² and the Gaia DR2 parallax ($3.676 \pm 0.021 \text{ mas}$; Gaia Collaboration 2018), we obtain a stellar age of $1.03 \pm 0.43 \text{ Gyr}$, a stellar mass of $1.38 \pm 0.02 M_\odot$, and a stellar radius of $1.44 \pm 0.03 R_\odot$, also consistent with the values reported by Delrez et al. (2016). The results are shown in Table 2.

3.1. Fourier transform of the CCF

Because of the moderate value of $v \sin i = 11.8 \text{ km s}^{-1}$ found with the spectral analysis, we also calculated it by means of the Fourier transform of the mean line profile (e.g., Dravins et al. 1990). This method can be used when the stellar $v \sin i$ is much greater than the width of the instrumental profile, typically for stars with $v \sin i \gtrsim 10 \text{ km s}^{-1}$ (Reiners & Schmitt 2002). We used the CCF as mean line profile since it has been proven to be a good mean line profile indicator for this kind of study (Borsa et al. 2015). The q positions of the first zeros of the Fourier transform give an estimate of the projected rotational velocity $v \sin i$, while the ratio q_2/q_1 is a direct indicator for solar-like differential rotation (equator rotating faster than poles; Reiners & Schmitt 2002). We found $v \sin i = 11.90 \pm 0.31 \text{ km s}^{-1}$ and $q_2/q_1 = 1.43 \pm 0.28$. By adopting an inclination angle for the star $i_\star = 8.1^\circ$ (Bourrier et al. 2020) and using the q_2/q_1 value, we computed the differential rotation parameter α by following Reiners & Schmitt (2003). We found $\alpha = 0.06 \pm 0.03$, compatible with the value $\alpha = 0.08^{+0.11}_{-0.13}$ obtained by Bourrier et al. (2020) with the study of the reloaded RM effect, thus excluding high differential rotation rates. We note that differential rotation can contribute to the RM shape (e.g., Serrano et al. 2020), in particular for polar orbit planets like WASP-121b. However, given its low rate for WASP-121, it is unlikely that it plays a major role in this context, but it could explain some of the RV fit residuals (Sect. 4.1).

¹ publicly available at www.eso.org/sci/software/pipelines/espresso/espresso-pipe-recipes.html

² http://stev.oapd.inaf.it/cgi-bin/param_1.3

Table 1. WASP-121 ESPRESSO observations log.

Night	Exp time	Mode	fiber B	S/N ¹ @550nm	Time on target [hours]	N _{spectra}	Seeing _{ave} [arcsec]
06 Jan 2019	400 s	1-UT HR21	Sky	~45	6.3	52	0.83
30 Nov 2018	300 s	4-UT MR42	Fabry-Perot	~180	2.7	29	0.79

¹per pixel extracted.

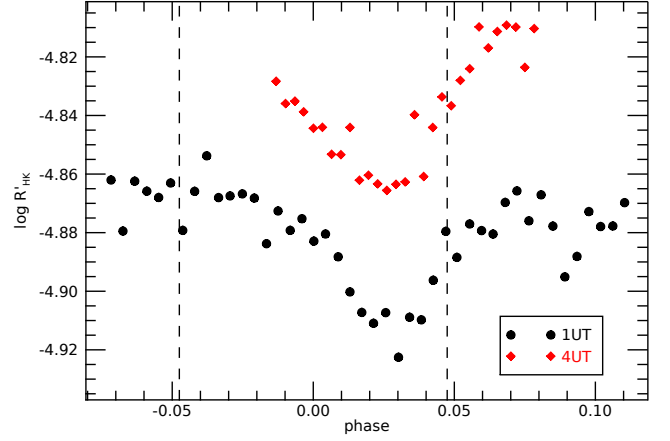
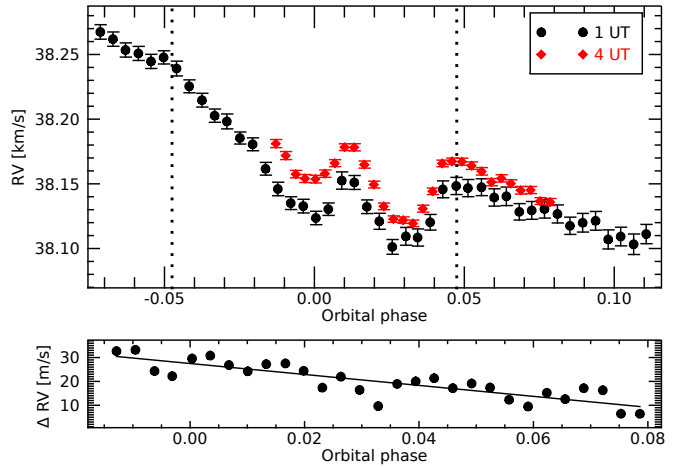
Table 2. Properties of the WASP-121 system.

Parameter	Value	Reference
WASP-121		
<i>Stellar parameters</i>		
T [K]	6586 ± 59	This work
log g	4.47 ± 0.08	This work
Fe/H	0.13 ± 0.04	This work
$v \sin i$ [km s ⁻¹]	11.8 ± 0.2	This work
M_s [M _⊙]	1.38 ± 0.02	This work
R_s [R _⊙]	1.44 ± 0.03	This work
age [Gyr]	1.03 ± 0.43	This work
<i>Orbital parameters</i>		
Period [days]	1.27492504 ^{+1.5×10⁻⁷} _{-1.4×10⁻⁷}	Bourrier et al. (2020)
T_0 [BJD]	2458119.72074 ± 0.00017	Bourrier et al. (2020)
R_p/R_s	0.12534±0.00005	Bourrier et al. (2020)
a/R_s	3.8131 ^{+0.0075} _{-0.0060}	Bourrier et al. (2020)
e	0.0	assumed
i [degrees]	88.49 ± 0.16	Bourrier et al. (2020)
V_{sys} [km s ⁻¹]	38.198 ± 0.002	This work
M_p [M _{Jup}]	1.157 ± 0.070	Bourrier et al. (2020)
K_s [km s ⁻¹]	0.177±0.008	Bourrier et al. (2020)
<i>RM+RM_{atmo} fit</i>		
μ	0.68 ^{+0.09} _{-0.08}	This work
λ [degrees]	-87.08 ^{+0.29} _{-0.27}	This work
$v \sin i$ [km s ⁻¹]	15.4±0.8	This work
$R_{p,\text{atmo}}/R_s$	-0.044 ^{+0.003} _{-0.004}	This work
delay [phase]	0.0029 ^{+0.0005} _{-0.0008}	This work
a/R_s ratio	2.61 ^{+0.21} _{-0.13}	This work

3.2. Stellar activity

Given the difference in the RV slope (see Sect. 4) and the possible different line contrast observed in the planetary absorptions of the two transits (see Sect. 5.2), we calculated the level of stellar activity $\log R'_{\text{HK}}$ (Noyes et al. 1984) for each transit, using the HARPS index calibration of Astudillo-Defru et al. (2017) as the one for ESPRESSO is still not available (Faria et al. 2020). Since there is a strong in-transit planetary signal in the core of the Ca II H&K lines (Fig. 1, see also Sect. 5.2), for each transit we average the $\log R'_{\text{HK}}$ values calculated on the out-of-transit spectra only. We find $\log R'_{\text{HK}} = -4.87 \pm 0.01$ and $\log R'_{\text{HK}} = -4.81 \pm 0.01$ for the 1-UT and 4-UT transits, respectively. The star is thus more active during the partial transit observed with the 4-UT mode. We note that stellar activity can change RM shape and/or out of transit RV slope significantly (Oshagh et al. 2018).

The in-transit behavior of the $\log R'_{\text{HK}}$ index (Fig. 1), which shows the same pattern in both transits, is likely due to the passage of the planet combined with atmospheric absorption in the Ca II H&K lines (Sect. 5.2). It is however interesting to note one


Fig. 1. $\log R'_{\text{HK}}$ activity indices calculated for the two transits. Vertical dotted lines show the expected beginning and end of the transit. Phase 0 represents the mid-transit time.

Fig. 2. (Top panel) ESPRESSO radial velocities of the WASP-121b transits observed. Vertical dotted lines indicate the expected beginning and end of the transit. (Bottom panel) RV difference between the two transits, calculated by quadratically interpolating the 1-UT RVs on the 4-UT phases. The black line shows the fitted linear trend with a slope significant at the 4.5σ level. An offset is expected because of the different instrumental setups used in the two transits.

thing: the rotation period of the star is ~1.13 days (Delrez et al. 2016; Bourrier et al. 2020), derived from spectroscopy, while TESS photometry showed a similar periodicity at ~1.16 days (Bourrier et al. 2020). If the stellar rotation period were 1.1554 days, then the star would have accomplished exactly 32 rotations between the two observations, and thus the planet could also be blocking the same active region on the stellar surface at the two transits.

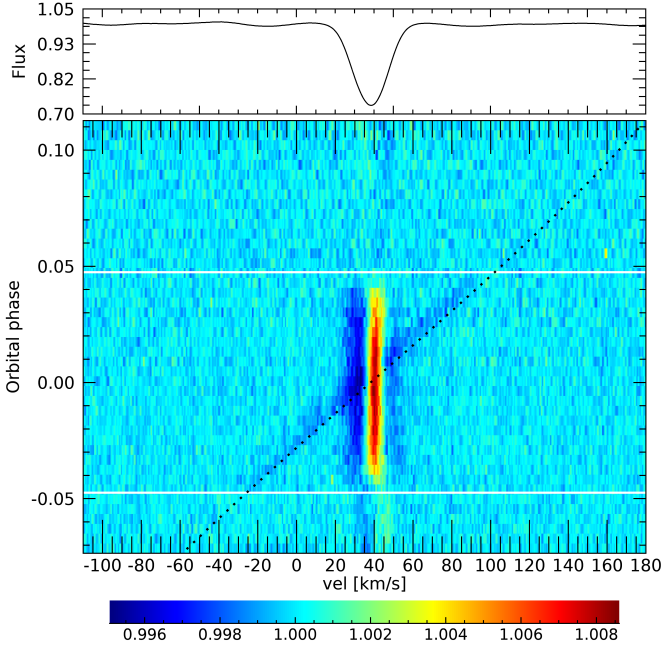


Fig. 3. (Top panel) Average out-of-transit stellar CCF. (Bottom panel) Tomography of CCF residuals for the 1-UT transit, in the stellar rest-frame. The stellar systemic velocity V_{sys} is still not subtracted. Horizontal white lines represent the beginning and end of the transit. The dotted black line shows the theoretical planetary RV. Differences between the stellar CCF residuals before and after the transit, possibly due to stellar activity, are noticeable.

4. Radial velocities and CCFs analysis

The RVs were extracted with a F9 stellar mask using the DRS version 2.0.0, with a step of 0.5 km s^{-1} (1.0 km s^{-1} for the 4-UT data) and using a broad velocity range for the CCF $[-150, 150] \text{ km s}^{-1}$ due both to the moderate projected rotational velocity of the star ($\sim 12 \text{ km s}^{-1}$, Sect. 3) and to check for the possible presence of any planetary signal whose lines should fall several dozens of km s^{-1} away from the stellar line. A list of the RVs is presented in Table 3. At first look the RVs present a clearly anomalous in-transit curve (Fig. 2), which is not predicted by any model of classic RM effect (e.g., Winn et al. 2008). Looking together at the RV curve and the CCF residuals tomographic map (CCFs divided by an average out-of-transit CCF, Fig. 3), we investigated the possibility of an extreme case of atmospheric RM effect.

4.1. Atmospheric Rossiter-McLaughlin effect

The atmospheric RM effect (Borsa et al. 2019) is a deviation of the in-transit RVs from the classical RM effect that happens when the atmosphere of the planet is intercepted by the mask used to create the stellar CCFs. By studying the shape of this deviation we can measure the extension of the planetary atmosphere that correlates with the stellar mask. When comparing the 1-UT and 4-UT RVs, we find a difference in the RV slope (Fig. 2, bottom panel). Even including the RV offset given by the two different instrumental setups, this slope difference amounts to $\sim 20 \text{ m s}^{-1}$ in ~ 3 hours and has a 4.5σ significance. When subtracting this slope (i.e., the linear trend fitted in Fig. 2, bottom panel), the two RV curves are fully compatible within the error bars. We cannot exclude that this is caused by the presence of additional bodies in the system, although Bourrier et al. (2020)

Table 3. ESPRESSO RV observations of WASP-121.

Time [BJD-2450000]	RV [km s^{-1}]	RV error [m s^{-1}]	Mode
8453.73466	38.1811	3.2	4-UT
8453.73889	38.1719	3.1	4-UT
8453.74314	38.1575	2.9	4-UT
8453.74709	38.1541	3.1	4-UT
8453.75150	38.1536	3.0	4-UT
8453.75556	38.1579	2.8	4-UT
8453.75972	38.1660	2.7	4-UT
8453.76391	38.1783	2.6	4-UT
8453.76804	38.1783	2.8	4-UT
8453.77230	38.1649	2.8	4-UT
8453.77636	38.1494	2.6	4-UT
8453.78054	38.1326	2.6	4-UT
8453.78466	38.1228	2.4	4-UT
8453.78883	38.1219	2.5	4-UT
8453.79297	38.1194	2.5	4-UT
8453.79720	38.1308	2.7	4-UT
8453.80133	38.1442	2.5	4-UT
8453.80543	38.1658	2.6	4-UT
8453.80959	38.1674	2.5	4-UT
8453.81379	38.1671	2.7	4-UT
8453.81790	38.1641	2.9	4-UT
8453.82214	38.1597	2.9	4-UT
8453.82636	38.1513	2.8	4-UT
8453.83054	38.1542	2.8	4-UT
8453.83462	38.1502	2.9	4-UT
8453.83877	38.1450	2.9	4-UT
8453.84302	38.1452	2.8	4-UT
8453.84706	38.1367	2.6	4-UT
8453.85128	38.1360	2.7	4-UT
8490.63286	38.2674	5.6	1-UT
8490.63824	38.2619	5.5	1-UT
8490.64356	38.2535	5.5	1-UT
8490.64904	38.2508	5.4	1-UT
8490.65438	38.2446	5.5	1-UT
8490.65977	38.2478	5.1	1-UT
8490.66527	38.2391	5.7	1-UT
8490.67063	38.2254	5.0	1-UT
8490.67609	38.2147	5.3	1-UT
8490.68146	38.2027	5.1	1-UT
8490.68666	38.1982	5.8	1-UT
8490.69221	38.1854	4.7	1-UT
8490.69763	38.1806	5.0	1-UT
8490.70312	38.1617	4.9	1-UT
8490.70834	38.1460	5.2	1-UT
8490.71383	38.1351	4.9	1-UT
8490.71914	38.1328	5.3	1-UT
8490.72452	38.1236	5.2	1-UT
8490.72979	38.1304	4.8	1-UT
8490.73552	38.1526	6.7	1-UT
8490.74084	38.1511	5.4	1-UT
8490.74618	38.1323	5.3	1-UT
8490.75148	38.1210	6.2	1-UT
8490.75699	38.1012	5.7	1-UT
8490.76278	38.1094	6.9	1-UT
8490.76778	38.1085	6.6	1-UT
8490.77311	38.1203	6.0	1-UT
8490.77848	38.1458	6.5	1-UT
8490.78417	38.1484	6.6	1-UT
8490.78917	38.1467	6.6	1-UT
8490.79492	38.1474	6.5	1-UT
8490.80032	38.1395	6.7	1-UT
8490.80551	38.1404	7.2	1-UT
8490.81100	38.1284	6.3	1-UT
8490.81630	38.1295	6.9	1-UT
8490.82171	38.1306	7.1	1-UT
8490.82723	38.1267	7.0	1-UT
8490.83255	38.1176	6.7	1-UT
8490.83795	38.1199	7.2	1-UT
8490.84344	38.1214	7.2	1-UT
8490.84880	38.1070	7.4	1-UT
8490.85412	38.1093	7.2	1-UT
8490.85964	38.1033	7.9	1-UT

analyzed three transits with HARPS without finding evidence of any changing slope. One more possibility is the different levels

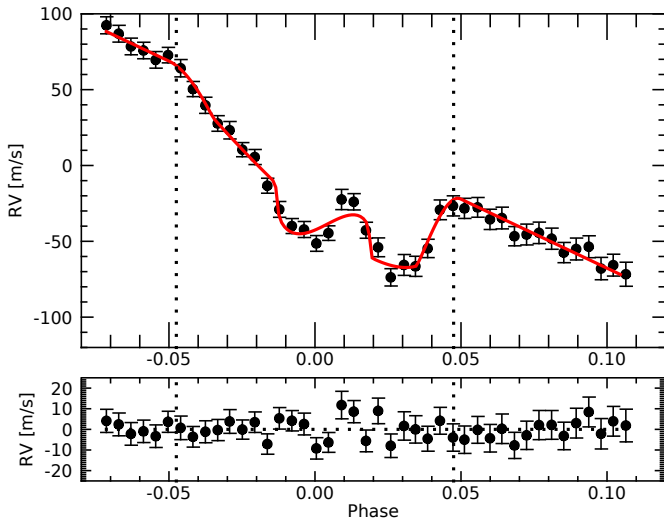


Fig. 4. RVs of the 1-UT transit together with the RM + atmospheric RM fit performed. The residuals are shown in the bottom panel.

of stellar activity of the star during the two transits (see Sect. 3.2). Since our aim is to analyze the in-transit RVs, we detrend the data from the Keplerian motion by fitting a linear model on the out-of-transit RVs, and subtract the fit result from the data. We limit our atmospheric RM analysis of the RVs to the complete 1-UT transit. The incompleteness of the 4-UT transit is a major obstacle in constraining the whole set of parameters of our model.

In Borsa et al. (2019), we first subtracted the best fit RM model with literature parameters from the data, and then fitted the atmospheric RM. Here instead we fit a model that is the sum of two RMs. The first is the classic RM (taken from Ohta et al. 2005), where as planet-to-star radius ratio (R_p/R_s) we use the sum of the R_p/R_s calculated in the literature from the photometric transits and the $R_{p,atmo}/R_s$ described below. This is to take into account the effects of the atmosphere on the classic RM. An increase in the apparent R_p/R_s because of the atmosphere is the same effect that causes the chromatic RM (Snellen 2004; Dreizler et al. 2009; Di Gloria et al. 2015), which in this case affects the whole wavelength range and thus is not visible as wavelength dependent. The second is the atmospheric RM. The atmospheric RM is basically a RM-like model, where the ratio $R_{p,atmo}/R_s$ is related to the extension of the atmosphere of the planet as if it were a disk. By definition, during a transit the planet (and thus the planetary atmosphere) travels from negative to positive RVs, following the Keplerian motion. If we consider that in the central part of the transit this can be approximated well by a straight line, this is the same as the Doppler shadow of an aligned planet, but since the perturbation on the CCF of the atmosphere is opposite (i.e., an excess absorption, as opposed to the Doppler shadow) its effect on the RVs will also be the opposite. We thus use a RM-like model (but with a different transit duration; see the description of the *ratio* parameter below) with the spin-orbit angle of the atmospheric track (λ_{atmo}) fixed to 180° . We also include other two parameters. The first is *delay*, which is related to the blueshift of the atmospheric signal. If the atmospheric track presents a blueshift, as is often observed for exoplanets with transmission spectroscopy (e.g., Ehrenreich et al. 2020; Bourrier et al. 2020), the RV of the atmosphere at the center of the transit will not be at zero. This will cause a delay in the atmospheric RM, making its center to be slightly postponed

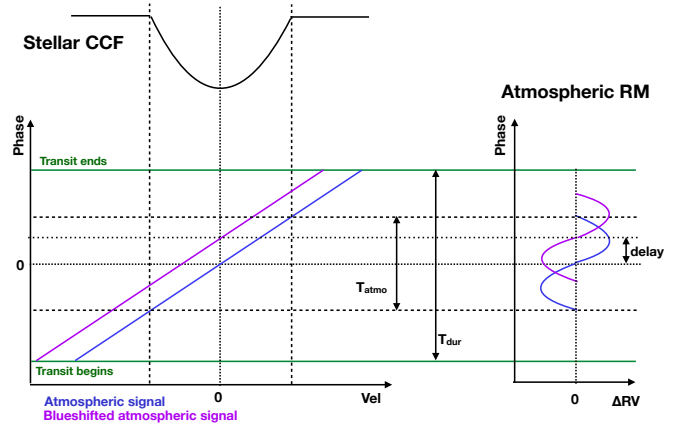


Fig. 5. Schematic view of the atmospheric RM effect.

with respect to the center of the transit. The *delay* parameter is thus the phase shift related to the average blueshift of the atmospheric signal. The second parameter we include here is *ratio*, which is the ratio of the true a/R_s parameter (with a the semi-major axis) of the planet to the a/R_s that describes the passage of the atmospheric track over the stellar CCF. This is basically the ratio of the duration of the classic RM to that of the atmospheric RM (T_{dur}/T_{atmo} in Fig. 5) as the transit duration is proportional to a/R_s (e.g., Seager & Mallén-Ornelas 2003). We leave *ratio* as a free parameter in the fit because we do not know a priori the width of the atmospheric signal, and so where its impact starts and ends at the edges of the CCF when extracting the RVs. We let the data tell us this in this way. We note that in our model we are assuming for simplicity (and because of the limited duration of the transit) that the atmospheric signal is constant both in amplitude and blueshift during the transit. A schematic view of the atmospheric RM and of the described parameters is presented in Fig. 5.

We fitted the RVs in a Bayesian framework by employing a differential evolution Markov chain Monte Carlo (DE-MCMC) technique (Ter Braak 2006; Eastman et al. 2013), running five DE-MCMC chains of 100,000 steps and discarding the burn-in. The medians and the 15.86% and 84.14% quantiles of the posterior distributions were taken as the best values and 1σ uncertainties. We fixed R_p/R_s , i , t_0 , and a/R_s to the values listed in Table 2. We left as free parameters the linear limb darkening coefficient μ , the spin-orbit angle λ , $v \sin i$, the atmospheric $R_{p,atmo}/R_s$, *delay*, and *ratio*. Priors for μ and λ were set to the values in Bourrier et al. (2020), for $v \sin i$ to the value determined in Sect. 3, and for the other three parameters to the result of a fit performed with the MPFIT IDL routine.

In Fig. 4 we show the fit results and the residuals. We note that the two RV points that deviate most from the fit are those taken while the planetary atmospheric track overlaps the Doppler shadow, as is also seen in the case of KELT-9b (Borsa et al. 2019). We find the sky-projected obliquity $\lambda = -87.08^{+0.29}_{-0.27}$, in agreement with Bourrier et al. (2020, $\lambda = 87.2 \pm 0.4$, -87.2 ± 0.4 translated in our reference system). The value of stellar $v \sin i = 15.4 \pm 0.8$ km s $^{-1}$ is larger than that retrieved from spectral analysis, we note however that different RM models are known to produce $v \sin i$ measurements often in disagreement with each other and with estimates obtained from spectral line broadening (Brown et al. 2017). We can translate the $delay = 0.0029^{+0.0005}_{-0.0008}$ into an average blueshift of the planetary atmospheric track -4 ± 1 km s $^{-1}$. The value $ratio = 2.61^{+0.21}_{-0.13}$

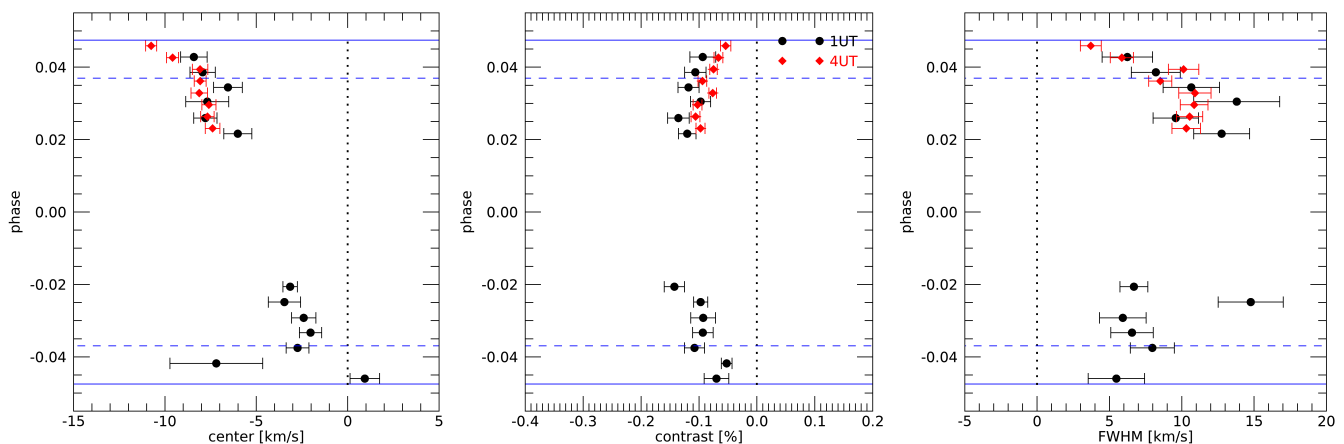


Fig. 6. Center (*left panel*), contrast (*central panel*), and width (*right panel*) of the in-transit atmospheric CCFs Gaussian fits as a function of the orbital phase. Horizontal blue lines show the transit duration, dashed blue lines show the full-transit limits. Measurements are not done where the atmospheric track is superimposed on the Doppler shadow.

measures the ratio between the durations of the RM and atmospheric RM effects. The atmospheric extension measurement is $R_{p,atmo}/R_s = -0.044^{+0.003}_{-0.004}$. Following Borsa et al. (2019) from this value we measured the height of the planetary atmosphere correlating with the stellar mask, which is $R_{atmo} = 1.052 \pm 0.015 R_p$. This height represents the extension of Fe I in the atmosphere, as the stellar mask used to compute the CCF is mainly composed of Fe I lines (which represent $\sim 76\%$ of the weighted spectroscopic information of the mask; Ehrenreich et al. 2020). This value is in agreement with the results from Gibson et al. (2020, Fe I present in low layers of the atmosphere) and Cabot et al. (2020, $R_{FeI} \sim 1.03 R_p$), which measured Fe I in the atmosphere by means of cross-correlation with theoretical templates.

Although the Doppler shadow is indeed larger than the atmospheric signal, we note that the RV deviation given by the atmospheric RM is of the same order of magnitude as the value given by the classic RM. This can happen because the Doppler shadow in this orbital configuration (almost polar projected orbit) is always close to the center of the CCF, while the atmospheric signal moves along it from the far left to the far right, and (even if much smaller) this results in a RV deviation almost as large as the one given by the Doppler shadow.

4.2. Planetary CCF

The planetary atmospheric track shown in Fig. 3 is slightly shifted from the theoretical planetary velocity computed with the orbital parameters of Table 2. ESPRESSO has recently proven its capability to resolve time variations of this atmospheric track (Ehrenreich et al. 2020). For WASP-121b, Bourrier et al. (2020) found a similar behavior. We thus investigated this with our data, by fitting a Gaussian profile to each atmospheric line profile in the planetary restframe. Errors on the CCF residuals were set to the standard deviation of their continuum. We excluded the part of the transit where the atmospheric track overlaps the Doppler shadow (see Ehrenreich et al. 2020). The results are shown in Fig. 6. The velocity center of the atmospheric track changes with time (Fig. 6, left panel), becoming more blueshifted in the second part of the transit, in a way similar to what happens in the case of the ultra-hot gas giant WASP-76b (Ehrenreich et al. 2020). This is confirmed by the agreement between the 1-UT and 4-UT data, unfortunately only possible for the second

part of the transit. We measure an average change in blueshift from $-2.80 \pm 0.28 \text{ km s}^{-1}$ in the first half to $-7.66 \pm 0.16 \text{ km s}^{-1}$ in the second half, excluding the ingress and egress. The results are close to those of Bourrier et al. (2020), who discovered that the atmospheric signal was becoming more blueshifted from the first to the second part of the transit. While we find no differences in the atmospheric CCF contrast (1050 ± 80 versus 970 ± 30 ppm), its width increases but not significantly (7.3 ± 0.7 versus $10.2 \pm 0.4 \text{ km s}^{-1}$). The contrasts can be translated into an effective planetary radius of $\sim 1.03 R_p$ (see details in Sect. 6), which is in agreement with the R_{atmo} found with the RV analysis ($R_{atmo} = 1.052 \pm 0.015 R_p$), thus reinforcing the validity of the atmospheric RM method. The average blueshift values found with the two analyses are also consistent with each other.

5. Transmission spectrum

The transmission spectrum is extracted following basically the procedure of Wyttenbach et al. (2015), which was performed independently for each of the two transits. We first shift the spectra to the stellar restframe by using the Keplerian model of the system with the parameters of Table 2, then we normalized each spectrum. Telluric correction is performed by exploiting the scaling relation between airmass and telluric line strength (Snellen et al. 2008; Vidal-Madjar et al. 2010; Astudillo-Defru & Rojo 2013), rescaling all the spectra as if they were observed to the airmass of the transit center. We can perform telluric correction in the stellar restframe as the variation of the Barycentric Earth RVs during one night is well below the resolution of the instrument. Then we divided all the spectra by a master stellar spectrum created by averaging all the out-of-transit spectra. At this stage we find in the residual spectra a clear pattern of wiggles, which was already described in Tabernero et al. (2020). We correct for this pattern by fitting for a sinusoid with varying period, phase, and amplitude for each spectrum, with the fit performed independently for each wavelength region where we looked for spectral features. As a final step we move to the planetary restframe by shifting all the residual spectra for the theoretical planetary radial velocity (calculated with values from Table 2). The transmission spectrum is now created by averaging all the full-in-transit residual spectra. We note again that the spectral resolution is different for the two transits analyzed. In order to take

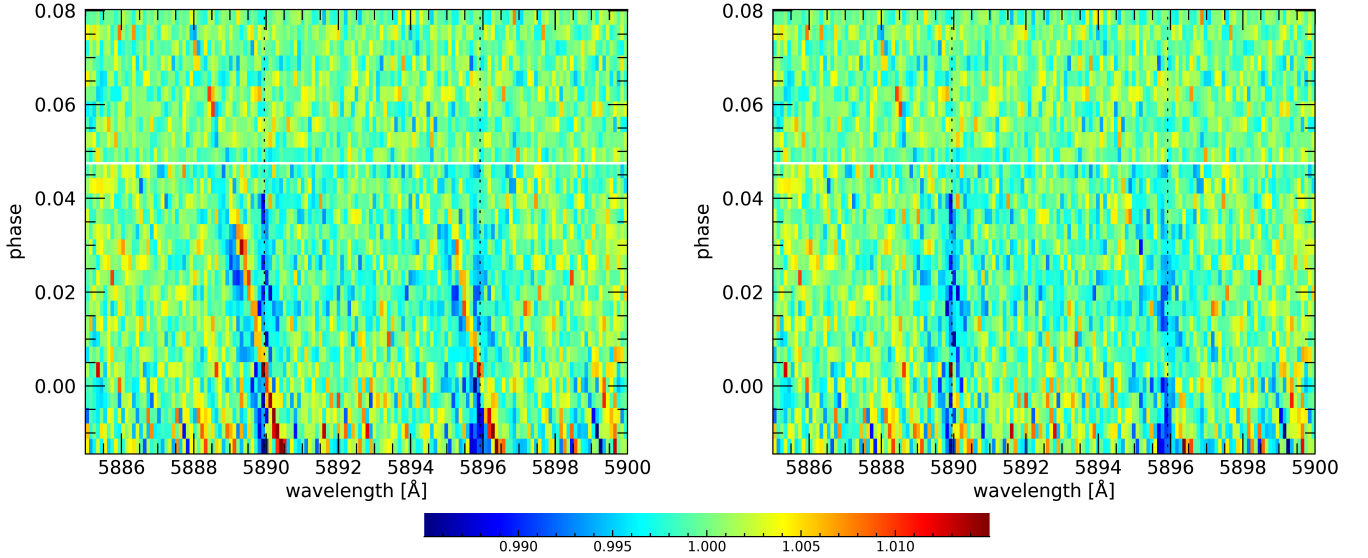


Fig. 7. Tomographic map of the sodium D doublet in the planetary restframe for the 4-UT transit, shown before (left panel) and after (right panel) the correction for the CLV and RM effects. The horizontal white line shows the end of the transit; the vertical dashed lines represent the planetary restframe of the sodium D lines.

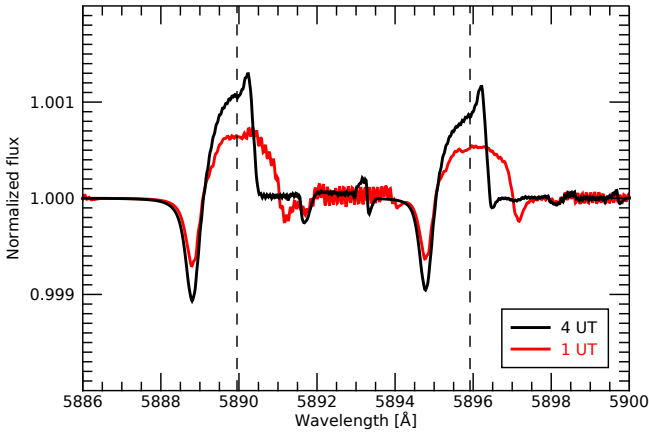


Fig. 8. Impact of CLV+RM effects on the transmission spectra of 1-UT (red line) and 4-UT (black line) observed transits in the wavelength region of the sodium D doublet.

this into account when estimating the significance of the detections in the transmission spectrum, the final rebinning is done with a wavelength step of 0.01 \AA for the 1-UT data and of 0.02 \AA for the 4-UT data. These values were chosen because they are very close to the mean resolution step calculated on the whole spectrograph in the two observing modes.

5.1. Stellar contamination in the transmission spectrum

The star in front of which the planet transits is not a simple homogeneous disk, but rotates and has a surface brightness that changes as a function of the distance from the center. Effects such as center-to-limb variation (CLV) and stellar rotation bring spurious signals in the transmission spectrum, possibly causing false detections (e.g., Casasayas-Barris et al. 2020) and incorrect line-profile estimations (e.g., Borsa & Zannoni 2018).

For the case of the WASP-121b transmission spectrum, these effects have been proven to be negligible while analyzing HARPS data (Cabot et al. 2020; Bourrier et al. 2020). Since with ESPRESSO we clearly see their impact in the 4-UT spectra (Fig. 7), we take them into account when analyzing our data. We thus created a model following the methodology of Yan et al. (2017). The star is modeled as a disk divided in sections of $0.01 R_s$. For each point we calculate the μ value ($\mu = \cos \theta$, with θ the angle between the normal to the stellar surface and the considered line of sight) and the projected rotational velocity (by rescaling the $v \sin i$ value of Table 2). Then we assign a spectrum to each point of the grid, by quadratically interpolating on μ and Doppler-shifting the model spectra created using the tool Spectroscopy Made Easy (SME, Piskunov & Valenti 2017), with ATLAS9 stellar atmospheric models (assuming solar abundances and local thermodynamic equilibrium approximation) and the line list from the VALD database (Ryabchikova et al. 2015). The model spectra are created for 21 different μ values and with null rotational velocity, and adapted to the resolving power of the instrument. Then we simulate the transit of the planet, calculating for different orbital phases the stellar spectrum as the average spectrum of the non-occulted modeled sections. We divide these for an average out-of-transit stellar spectrum, and we have as a result the simulated RM+CLV effects at each in-transit orbital phase. In Fig. 7 (right panel) we show in a 2D tomographic map the correction with our model applied to the 4-UT data in the wavelength zone of the sodium D doublet. We can calculate the impact on the average transmission spectrum by moving all the in-transit spectra in the planetary restframe and averaging them.

During the transit of a planet the occulted stellar regions are different. This means that the analysis of planetary transmission spectra which are calculated from complete or incomplete transits will be affected in a different way by the CLV and RM effects. In Fig. 8 we show their impact on the sodium D doublet wavelength region of the two ESPRESSO transmission spectra analyzed. The system orbital configuration makes the global effect larger by a factor ~ 2 for the 4-UT partial transit.

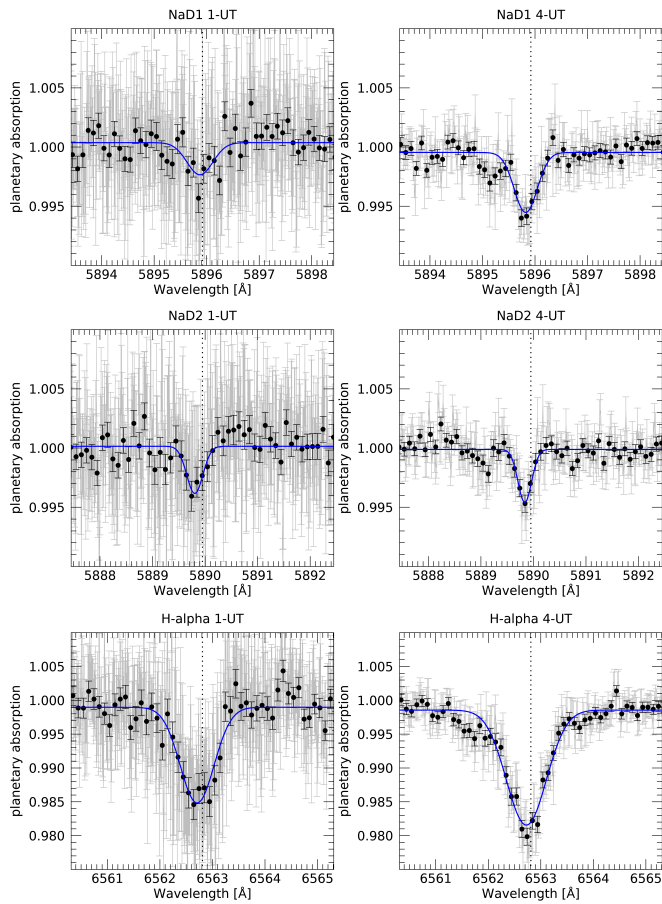


Fig. 9. Detections of Na D1 (first row), Na D2 (second row), and $H\alpha$ (third row) for the transits observed with 1-UT (first column) and 4-UT (second column). The vertical scale is the same for each row, showing the precision of the 4-UT data. The black points represent 0.1 Å binning; the blue line is the best fit Gaussian profile. The vertical dotted line shows the expected planetary restframe.

We note that Cabot et al. (2020) showed the non-impact of stellar effects CLV+RM on the transmission spectrum of WASP-121b retrieved using three HARPS transits. Our model is consistent with theirs, but given the higher quality of our ESPRESSO data (and in particular the high S/N of the 4-UT transit; see Fig. 7) we chose to remove stellar effects from the data. For uniformity in the analysis, we subtracted the CLV+RM model from the transmission spectra of both transits.

5.2. Detections of planetary absorption lines

We analyzed the transmission spectra retrieved in the two transits independently after the correction of the stellar RM+CLV effects because of the different resolving power of the two observing modes used and because of the difference in the stellar activity level (Sect. 3.2). A summary of the absorption lines detected in the planetary atmosphere is reported in Table 4. The parameters are calculated with a Gaussian fit and a MCMC error bar estimation. We report from the analysis of the two transits significant detections ($> 4\sigma$) for the previously detected Na D1, Na D2, and $H\alpha$ lines (Fig. 9), together with new detections of Ca II H&K (Fig. 10). Only in the 4-UT transit we can also detect Li, Mg I, and K (Fig. 11). We can detect only one line of the K doublet at ~ 770 nm (Table 4), as the other one falls in a region

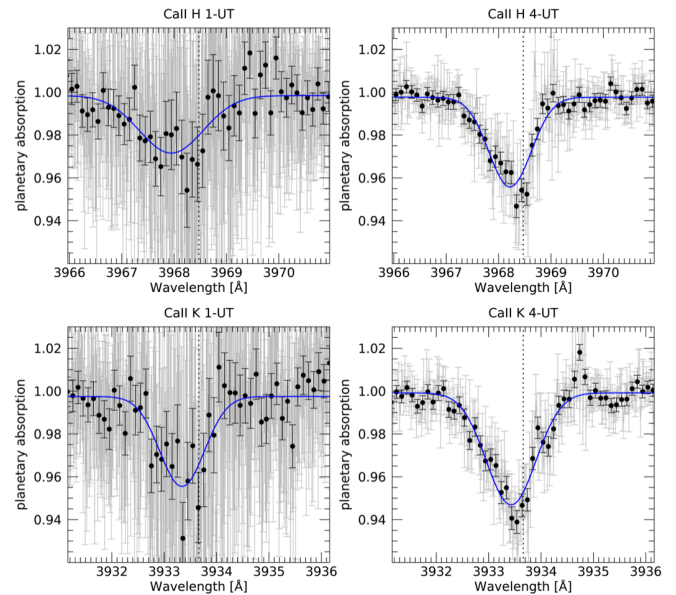


Fig. 10. New detections of Ca II H (first row) and Ca II K (second row) in the 1-UT and 4-UT transits (first and second column, respectively). The black points represent 0.1 Å binning; the blue line is the best fit Gaussian profile. The vertical dotted line shows the expected planetary restframe.

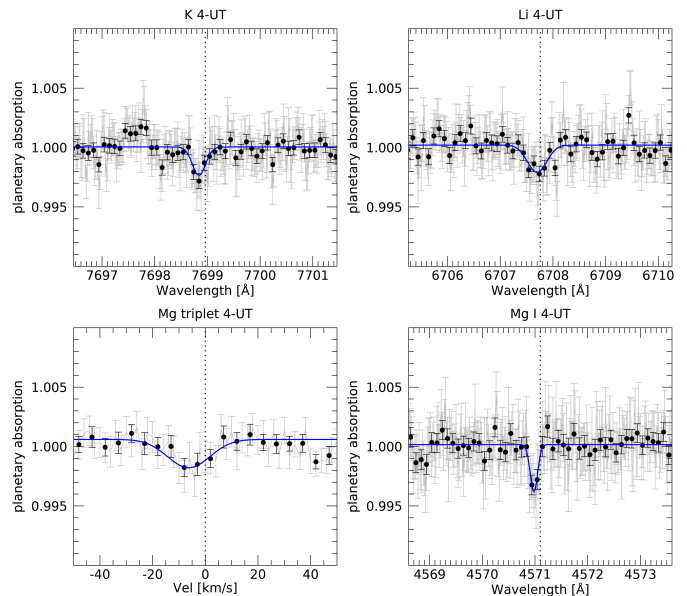


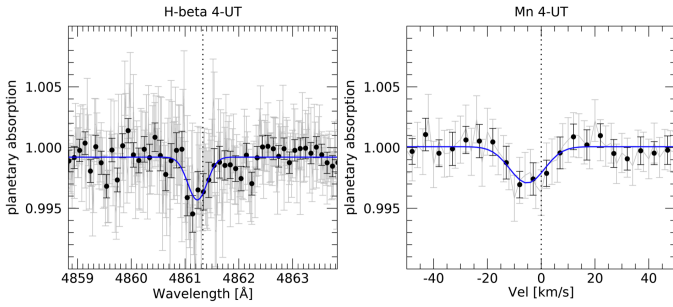
Fig. 11. New detections of K (top left), Li (top right), and Mg (bottom panels) in the 4-UT transit. The black points represent 0.1 Å (5 km s⁻¹ for Mg triplet) binning; the blue line is the best fit Gaussian profile. The vertical dotted line shows the expected planetary restframe.

of very strong telluric absorption. The Mg triplet is detected only when averaging the three lines in the velocity space. We also report on possible detections of $H\beta$ (3.2σ) and Mn triplet (3.3σ) (Fig. 12).

Checking the reference frame of the detections is mandatory when we want to be sure they are caused by the planetary atmosphere and not by spurious stellar effects (e.g., Brogi et al. 2016; Borsa & Zannoni 2018). For each element we thus also report whether the detection is resolved in the 2D tomographic map (Table 4 and Fig. 13). This quality check confirms that the

Table 4. Summary of the detections in the transmission spectra of the two transits. Detection is considered positive (Y) only at the level of 4σ and beyond, and partial (YN) in the range 2.5 - 3.9σ . “2D” refers to the visibility in the 2D tomographic map.

Element	λ_{air} [Å]	Contrast [%]	1-UT			Detection	4-UT			Detection	2D
			FWHM [km s ⁻¹]	Shift [km s ⁻¹]			FWHM [km s ⁻¹]	Shift [km s ⁻¹]			
Ca II K	3933.66	4.20 ± 0.70	76.63 ± 14.63	-24.40 ± 5.27	Y		5.22 ± 0.17	85.1 ± 3.1	-17.6 ± 1.4	Y	Y
Ca II H	3968.47	2.68 ± 0.51	108.73 ± 18.87	-39.67 ± 7.86	Y		4.18 ± 0.19	71.9 ± 3.7	-19.0 ± 1.6	Y	Y
Mn	4030.76	N/A	N/A	N/A	N		0.29 ± 0.08	15.3 ± 3.9	-5.2 ± 2.1	YN	N
	4033.07										
	4034.49										
Mg I	4571.10	N/A	N/A	N/A	N		-0.40 ± 0.08	10.9 ± 1.9	-7.9 ± 1.0	Y	N
H β	4861.33	N/A	N/A	N/A	N		0.35 ± 0.11	26.1 ± 14.9	-6.3 ± 4.3	YN	YN
Mg I	5167.32	N/A	N/A	N/A	N		-0.24 ± 0.06	13.4 ± 4.4	-6.3 ± 1.8	Y	Y
	5172.68										
	5183.60										
Na D2	5889.95	0.398 ± 0.081	18.42 ± 4.56	-7.42 ± 1.98	Y		0.447 ± 0.045	15.6 ± 1.9	-5.9 ± 0.8	Y	Y
Na D1	5895.92	0.271 ± 0.067	29.53 ± 9.94	-2.45 ± 3.18	Y		-0.51 ± 0.048	26.3 ± 3.3	-4.9 ± 1.1	Y	Y
H α	6562.81	1.414 ± 0.090	34.70 ± 2.65	-4.64 ± 1.18	Y		1.70 ± 0.048	40.9 ± 1.7	-3.9 ± 0.6	Y	Y
Li	6707.76	N/A	N/A	N/A	N		0.23 ± 0.04	19.4 ± 3.3	-2.7 ± 1.6	Y	Y
K	7698.96	N/A	N/A	N/A	N		0.23 ± 0.05	12.5 ± 5.4	-4.9 ± 1.2	Y	N

**Fig. 12.** Possible detections of H β and Mn triplet (averaged in the velocity space) planetary line profiles in the 4-UT transmission spectrum. The black points represent 0.1 Å binning (5 km s^{-1} for Mn); the blue line is the best fit Gaussian profile. The vertical dotted line shows the expected planetary restframe.

absorption is in the planetary restframe for all the significant detections except for K, which is in a wavelength region particularly affected by strong telluric contamination and so its rest-frame cannot be discriminated in the 2D map.

Each element line detected in the transmission spectra presents a net blueshift, that for the low layers of the atmosphere (thus excluding Ca II H&K and H α lines) on average is of $\sim 5 \text{ km s}^{-1}$, which is indicative of winds in the planetary atmosphere coming from the dayside to the nightside.

5.3. Cross-correlation with templates

We created WASP-121b high-resolution theoretical transmission spectra, expressed in planetary radius as a function of wavelength for different species of interest. Models of Fe I, Fe II, Ti I, Ti II, Cr I, V I, Ti O (Plez linelist), and VO (Plez linelist) were generated by using petitRADTRANS (Mollière et al. 2019), while those of CaH and ZrO were generated via TURBOSPECTRUM (Plez 2012). We assumed solar abundances, an isothermal atmospheric

profile with $T=3000 \text{ K}$ and a continuum pressure level of 1 mbar . These parameters were set because they are typical for UHJs (e.g., Hoeijmakers et al. 2019; Stangret et al. 2020). The atmospheric models were translated into flux $(R_p/R_s)^2$, convolved at the ESPRESSO resolving power and continuum normalized.

Cross-correlation between the data and the models is performed in the stellar restframe on single residual spectra after the removal of a master out-of-transit star and telluric contamination (with the procedures explained in Sect. 5) over the whole ESPRESSO wavelength range. We define the cross-correlation as

$$C(v, t) = \sum_{i=1}^N x_i(t, v) M_i, \quad (1)$$

where M is the model normalized to unity and x are the N wavelengths of the spectra taken at the time t and shifted at the velocity v . In this way we preserve the flux information (e.g., Hoeijmakers et al. 2019). In our analysis we set to zero all the model lines with contrast of less than 5% of the maximum in our wavelength range.

We selected a step of 0.5 km s^{-1} (1 km s^{-1} for the 4-UT) and a velocity range $[-200, 200] \text{ km s}^{-1}$. The spectra are divided into segments of 200 Å (see, e.g., Hoeijmakers et al. 2019), then the cross-correlation is performed for each segment. We performed a sigma-clipping at 5σ and masked the wavelength ranges most affected by telluric contamination (the intervals 5240 - 5280 Å , 6865 - 6930 Å , 7580 - 7700 Å). Then for each exposure we applied a weighted average between the cross-correlations of the single segments, where the weights applied to each segment are the inverse of its standard deviation (i.e., since we are in the photon-noise dominated regime, the higher the S/N, the greater the weight) and the depths of the lines in the model. For a range of K_p values from 0 to 300 km s^{-1} , in steps of 1 km s^{-1} , we averaged the in-transit cross-correlation functions after shifting them in the planetary restframe. This is done by subtract-

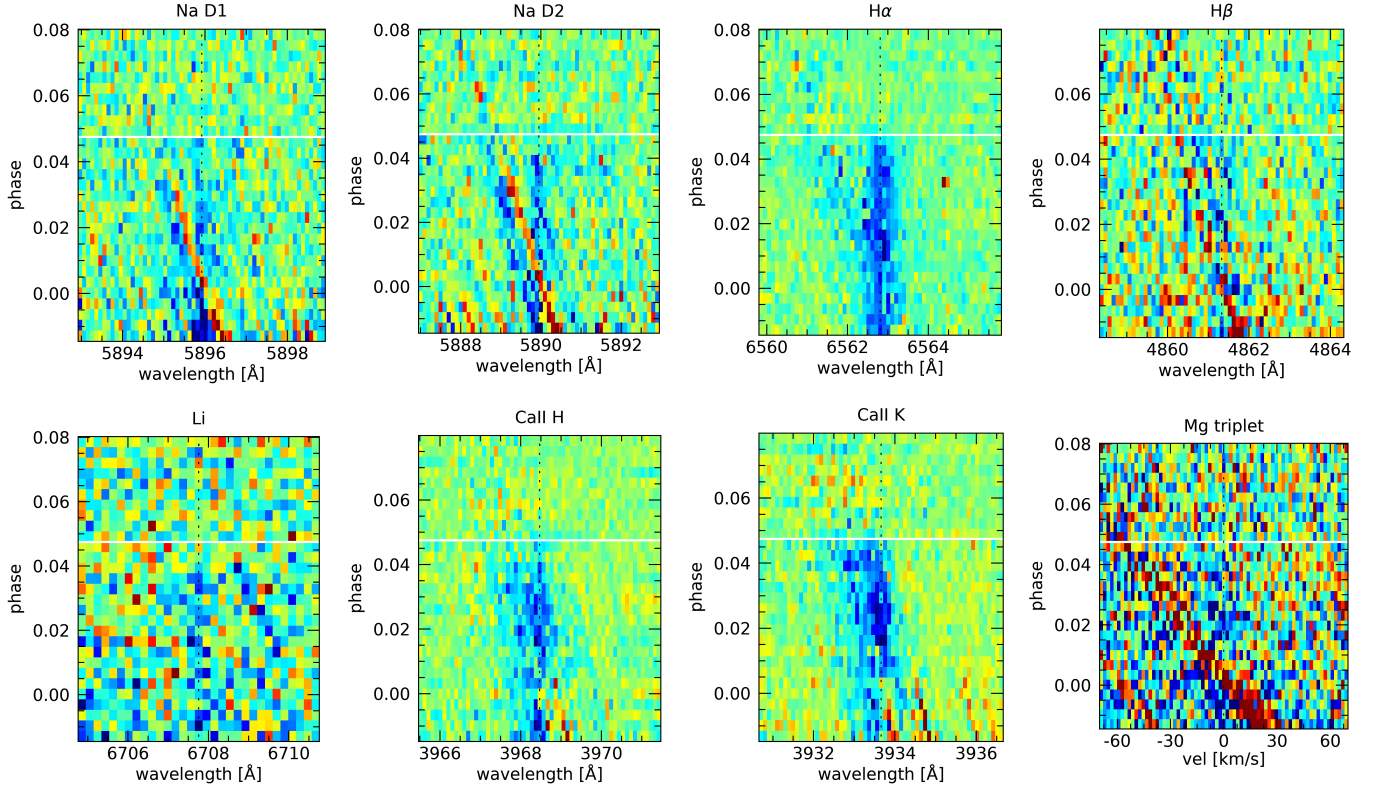


Fig. 13. Tomography positive quality checks of the detections in the planetary restframe, for the 4-UT partial transit, before applying the stellar contamination correction (this also shows the restframe of the Doppler shadow, i.e., the red track). Each square represents a 0.1 \AA bin on the horizontal scale (except 0.2 \AA for Li and 1 km s^{-1} for Mg). The color scale (not shown here as these are qualitative plots) is different for each plot, from blue representing absorption to red representing emission. The vertical dotted lines represent the laboratory wavelength. The horizontal white lines represent the end of the transit. The Mg tomography (bottom right plot) is presented in the velocity space as the sum of the three lines of the triplet.

Table 5. Summary of cross-correlation detections in the atmosphere of WASP-121b, with results for the 1-UT and 4-UT transits. Center and S/N are estimated for uniformity at the theoretical K_p value.

Element	K_p [km/s]	1-UT		K_p [km/s]	4-UT	
		center [km/s]	S/N@ $K_{p,\text{theoretical}}$		center [km/s]	S/N@ $K_{p,\text{theoretical}}$
Fe I	203^{+8}_{-9}	-7.5 ± 0.3	13.3 ± 0.6	208^{+18}_{-12}	-8.5 ± 0.5	8.6 ± 0.6
Fe II	195^{+12}_{-12}	-6.0 ± 0.8	4.4 ± 0.4	N/A	N/A	N/A
Cr I	203^{+8}_{-9}	-7.2 ± 0.7	4.2 ± 0.3	206^{+11}_{-13}	-9.1 ± 0.3	9.2 ± 0.3
V I	197^{+11}_{-7}	-7.2 ± 0.4	6.6 ± 0.3	214^{+23}_{-33}	-8.3 ± 0.5	5.5 ± 0.3

ing the planetary radial velocity calculated for each spectrum as $v_p = K_p \times \sin 2\pi\phi$, with ϕ the orbital phase. We thus created the K_p versus V_{sys} maps that are used to verify the real planetary origin of any possible signal. We evaluated the noise by calculating the standard deviation of the K_p versus V_{sys} maps, where $|V| > 70 \text{ km s}^{-1}$, i.e., far from where any stellar or planetary signal is expected. The significance of the detections (Table 5) was calculated by dividing the best K_p cross-correlation function for the noise, and by fitting a Gaussian function to the result.

We confirm previous detections of Fe I (Fig. 14), Cr I (Fig. 15), and V I (Fig. 16). We also confirm the presence of Fe II in the planetary atmosphere (Fig. 17), which has been previously debated (Ben-Yami et al. 2020; Hoeijmakers et al. 2020). A net blueshift is present for all the detections. We find no evidence

of the presence of Ti I (66 ppm at 3σ), Ti II (460 ppm), VO (18 ppm), TiO (12 ppm), CaH (36 ppm), or ZrO (20 ppm), given the accuracy of the linelists used.

In Table 5 we present a summary of the detections in the two transits. The best K_p is often lower than the theoretical value ($K_p \sim 218 \text{ km s}^{-1}$). This is possibly due to the atmospheric blueshift variability discussed in Sect. 4.2. It is interesting to note that while for Fe I, Fe II, and V I the detection significance (calculated at the theoretical K_p) is higher for the complete 1-UT transit (with no detection of Fe II with the 4-UT), it is the opposite for the case of Cr I. We recall that the two datasets were acquired with different resolving power ($R \sim 140,000$ for 1-UT versus $R \sim 70,000$ for 4-UT). We also note that the efficiency of the two observing modes is different, and in particular the tran-

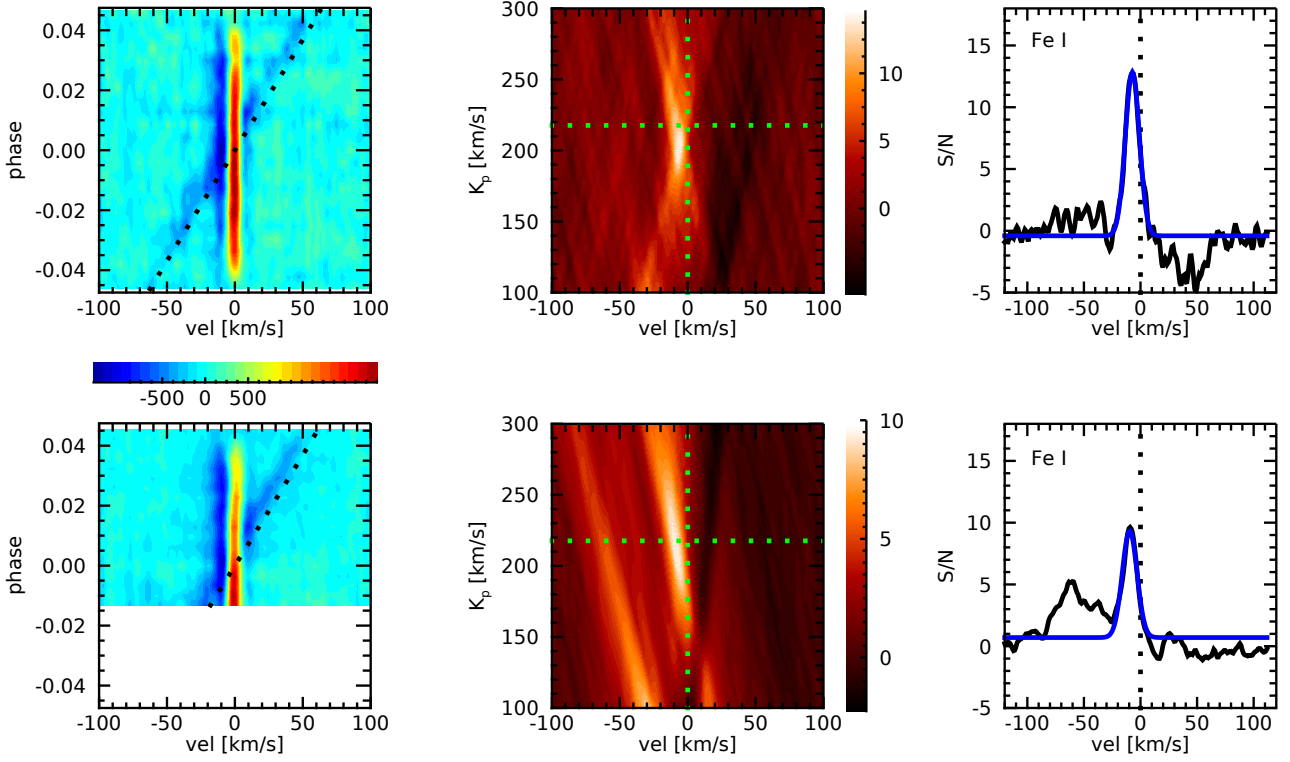


Fig. 14. Cross-correlation of the data with the Fe I model. Shown are the results for the 1-UT transit (top), and those for the 4-UT transit (bottom). The first column shows the contour plots of the temporal variation of the cross-correlation, with a dashed line to show the expected planetary velocity; the colorbar scale is in ppm. The second column is the K_p vs velocity map after summing the cross-correlations for different K_p , with colorbar scale in S/N. Green dashed lines are centered on the expected planetary position. The third column shows the final S/N of the detection, with the performed Gaussian fit in blue, as calculated at the theoretical K_p value.

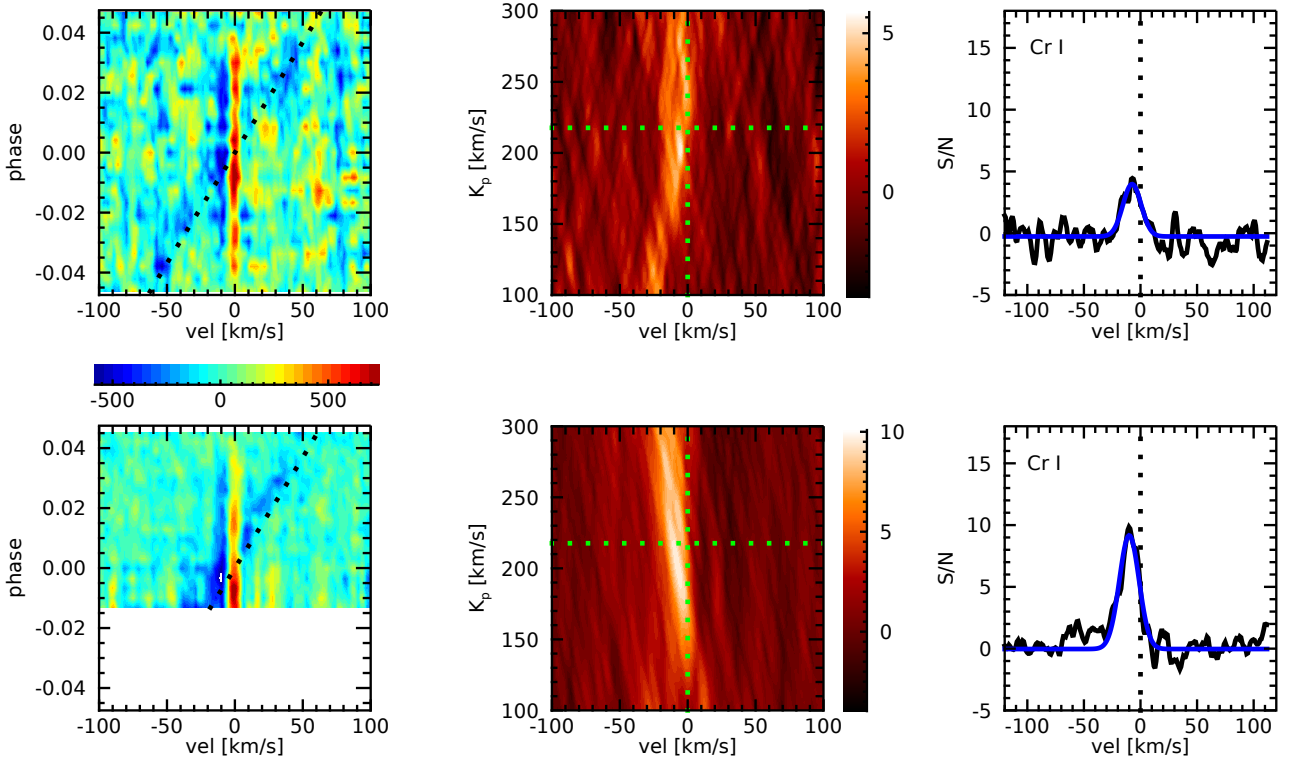


Fig. 15. Same as Fig. 14, but for Cr I.

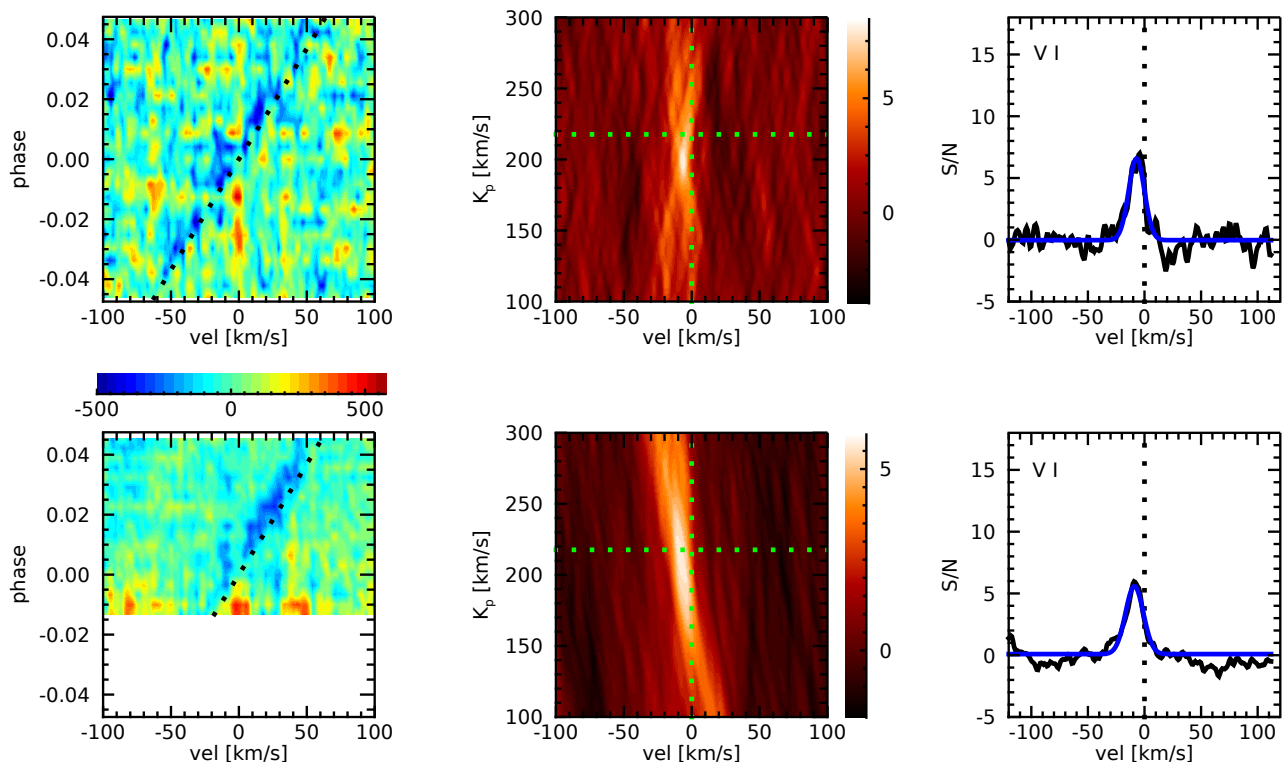


Fig. 16. Same as Fig. 14, but for V I.

sits were observed before the fiber upgrade (Pepe et al. 2020). It is hard in this case to make a direct comparison of what is better between resolving power and S/N when looking for species by using the cross-correlation technique since the two datasets are not compatible due to the incompleteness of the 4-UT transit. It is probable, however, that a combination of the two variables is a key factor, depending also on which wavelength region the lines of the species that are searched for fall into.

6. Discussion and conclusions

We observed two transits of the UHJ WASP-121b with ESPRESSO. By analyzing the strange shape of the in-transit RVs, we were able to prove that this is a case of atmospheric RM, showing the presence of (mostly) Fe in the planetary atmosphere and its blueshift by using only the stellar RVs. The atmospheric RM is confirmed to be a valid way to detect in the atmosphere of exoplanets lines that are present in the stellar mask used to calculate the RVs. By studying the exoplanet transmission spectrum, we more than doubled the number of previously detected atomic species in the atmosphere of WASP-121b, reinforcing previous detections of Na D1, Na D2, and H α , and adding Li, Mg, K, and Ca II H&K (and possibly H β and Mn). Lithium detection, despite its low amplitude ($\sim 0.2\%$), is significant at $> 6\sigma$ level. This is a remarkable result, considering that it is achieved with only one partial transit with the 4-UT mode and we were able to confirm it in the planetary restframe with the 2D tomography. This became possible thanks also to the fact that there is no lithium line in the stellar spectrum, thus we are working at the continuum level with a very high S/N. Lithium was first claimed in an exoplanetary atmosphere by Chen et al. (2018) for WASP-127b, but with low-resolution transmission spectroscopy (and not confirmed with high resolution, Allart et al. 2020). Tabernero et al. (2020) and this work present the first detections of Li in plan-

etary atmospheres at high resolution, also providing 2D tomographic evidence of their coherence with the planetary restframe. The detection of a trace element like Li in exoplanet atmospheres is an important step, as it can help in the understanding of planet formation history and lithium depletion in planet-hosting stars (e.g., Bouvier 2008; Israelian et al. 2009; Chen et al. 2018). We note that we cannot detect lithium in the 1-UT transit because of the insufficient S/N.

In Fig. 18 we show the effective planet radius for the detected elements, which is calculated assuming $R_{\text{eff}}^2/R_p^2 = (\delta + h)/\delta$, where δ is the transit depth (from Table 2) and h is the line contrast (e.g., Chen et al. 2020). As expected, features like Ca II and H α are present up to very high altitudes in the atmosphere, as in the case of other hot exoplanets (e.g., Yan & Henning 2018; Yan et al. 2019; Casasayas-Barris et al. 2019). The absorptions from Ca II H&K lines are very prominent, probing atmospheric layers close to and possibly beyond the planetary Roche radius ($R_{\text{Roche}} \sim 1.77 R_p$). As the Roche lobe is elongated toward the star, in a transiting configuration it extends to about 2/3 of the extension to the L1 Lagrange point (Vidal-Madjar et al. 2008), with an equivalent value of the transiting Roche lobe of $\sim 1.3 R_p$ for WASP-121b (Sing et al. 2019). Ionized species were already detected at these high altitudes in the atmosphere of WASP-121b with *HST* (Fe II and Mg II, Sing et al. 2019). When considering the equivalent Roche lobe radius, our detections of Ca II H&K and also H α are significantly beyond it at the 5.3σ , 5.9σ , and 6.2σ level, respectively, for the case of the 4-UT transit. We note that the model spectra we used for the CLV+RM effect correction could be imperfect in the core of chromospheric lines such as Ca II H&K (e.g., Casasayas-Barris et al. 2020). However, the presence of strong absorption in the planet atmosphere is certain as it is also confirmed by the 2D tomographic map (Fig. 13). The slight asymmetries observed on these line profiles (Fig. 10)

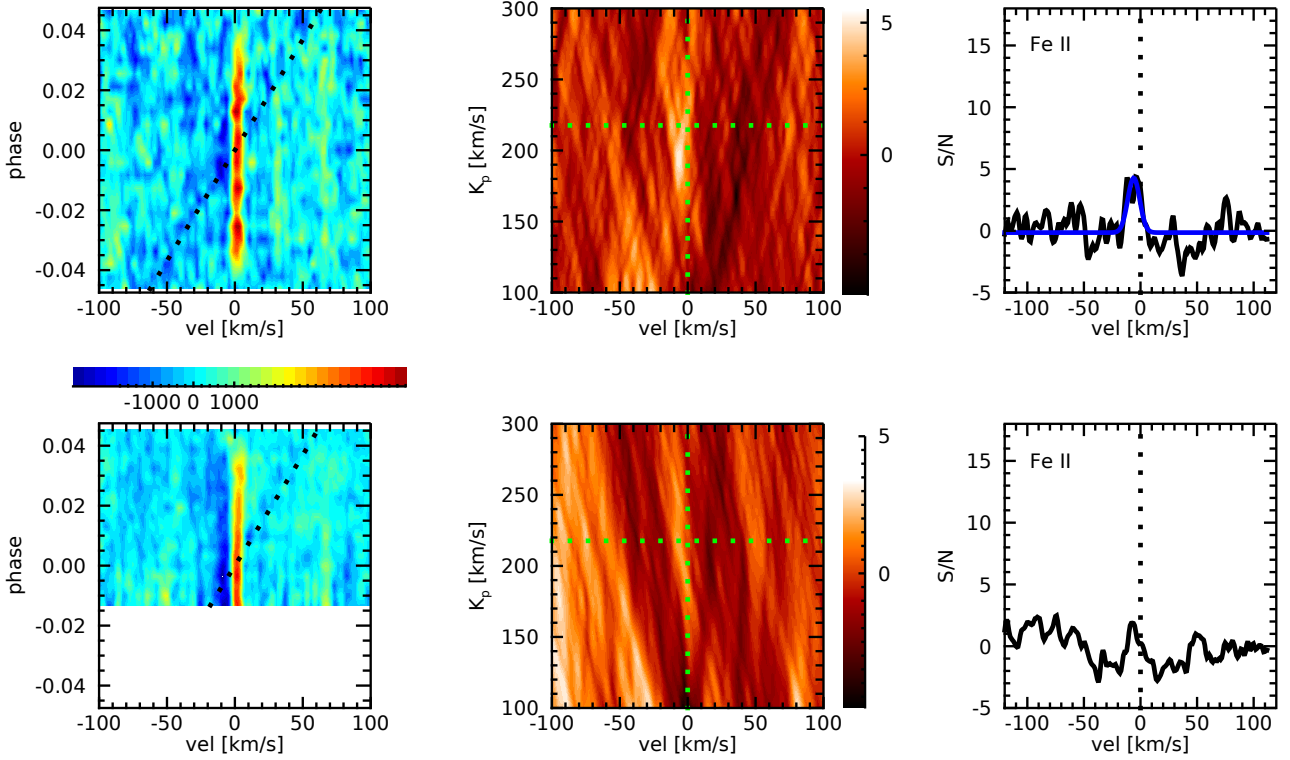


Fig. 17. Same as Fig. 14, but for Fe II.

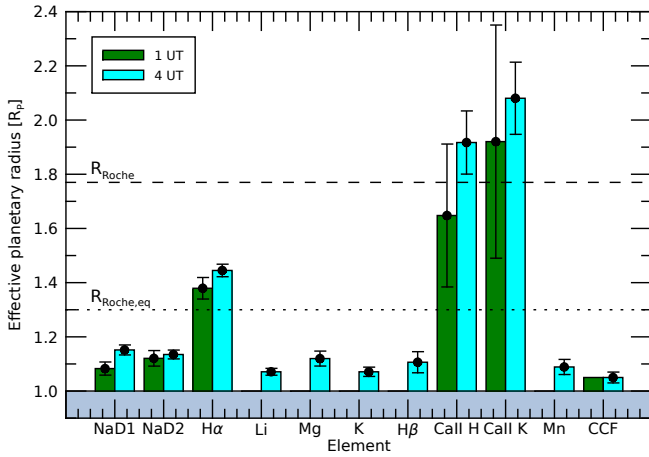


Fig. 18. Effective planetary radius for each element detected, shown for both the transits analyzed. Error bars refer to 1σ . The horizontal dashed and dotted lines represent respectively the Roche lobe radius of $1.77 R_p$ and the transit-equivalent Roche lobe radius for the transiting exoplanet case of $\sim 1.3 R_p$.

could be due to the extension beyond the Roche lobe radius, and thus could be probing an ongoing planetary atmospheric escape.

Our detections probe different layers of the atmosphere, thus we compared the retrieved line widths to those predicted for a tidally locked WASP-121b (Fig. 19). While for the low atmosphere tidally locked rotation can account for most of the thermal broadening (also pointed out in Bourrier et al. 2020), the full width at half maximum (FWHM) values of the deepest absorption lines H α and Ca II are significantly larger than those expected for a tidally locked rotating atmosphere. Tidally locked rotation is thus not the main source of atmospheric broadening

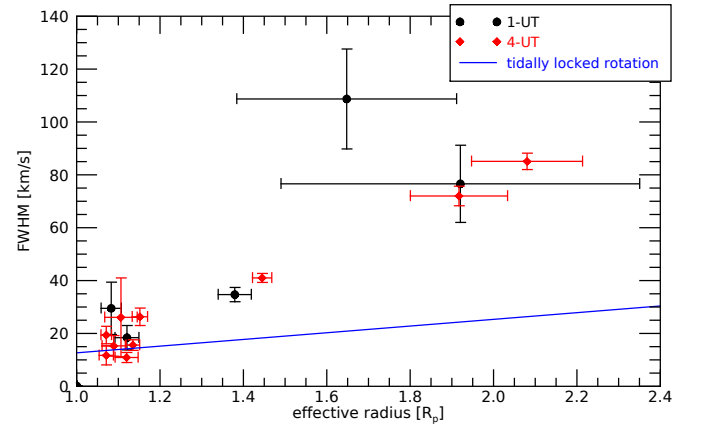


Fig. 19. Effective planetary radius vs FWHMs of the elements detected. The blue line shows the expected tidally locked planet's rotational broadening.

for the higher layers of the atmosphere. In addition, the blueshift of Ca II H&K is larger than for the other detected lines. The planet is probably experiencing atmospheric evaporation, thus the lines could be broadened by the expanding atmosphere via vertical winds or high-altitude jets.

We note that the line contrast of the detected atmospheric features is systematically (but not significantly) higher for the 4-UT data with respect to the 1-UT (Table 4, Fig. 18). This is hardly due to the different spectral resolution, as in this case we would expect an opposite behavior (i.e., lines becoming deeper with higher resolving power). One possible cause is the atmospheric blueshift variability during transit shown in Sect. 4.2. This in fact causes a spread of the lines when we sum all the single transmission spectra of the 1-UT transit. On the contrary, this

does not happen for the 4-UT data, as they are restricted to the second part of the full transit where the atmospheric restframe is almost constant (Fig. 6, left panel). One more possible interesting explanation could be the different level of stellar activity during the two transits, with the star being more active when we observe deeper planetary atmospheric lines. The contrast difference is seen for lines that are sensitive to stellar activity such as Na D, H α , and Ca II H&K. We do not know exactly the timescales necessary for the atmosphere to react to stellar activity changes, but the temporal distance of >1 month between the two observed transits could be more than enough.

With one partial transit with the 4-UT MR mode we could detect more elements than with one complete transit with the 1-UT HR mode. This is due to the very high S/N of the 4-UT data, which exploits the light coming from a 16m-equivalent telescope despite the lower resolving power ($R \sim 70,000$ versus $R \sim 138,000$). In this case the S/N overcomes the spectral resolution when looking for single lines of atomic species.

In conclusion, ESPRESSO is able to deeply investigate the atmospheres of exoplanets and temporally resolve the atmospheric behavior; it will play a major role in the coming years in the field of exoplanet characterization. Here we showed its potential applied to the atmospheric analysis of WASP-121b, which is confirmed to be one of the most intriguing UHJs and that definitely deserves future follow-up investigations.

Acknowledgements. We thank the referee for their useful comments that helped improving the clarity of the manuscript. The authors acknowledge the ESPRESSO project team for its effort and dedication in building the ESPRESSO instrument. FB acknowledges financial support from INAF through the ASI-INAF contract 2015-019-R0, and M. Rainer for helpful discussions on the Fourier transform of the CCF. This work has been carried out within the framework of the National Centre of Competence in Research PlanetS supported by the Swiss National Science Foundation. R. A. acknowledge the financial support of the SNSF. This work was supported by FCT - Fundação para a Ciência e a Tecnologia through national funds and by FEDER through COMPETE2020 - Programa Operacional Competitividade e Internacionalização by these grants: UID/FIS/04434/2019; UIDB/04434/2020; UIDP/04434/2020; PTDC/FIS-AST/32113/2017 & POCI-01-0145-FEDER-032113; PTDC/FIS-AST/28953/2017 & POCI-01-0145-FEDER-028953; PTDC/FIS-AST/28987/2017 & POCI-01-0145-FEDER-028987. O.D.S.D. is supported in the form of work contract (DL 57/2016/CP1364/CT0004) funded by FCT. This project has received funding from the European Research Council (ERC) under the European Union's Horizon 2020 research and innovation programme (project Four Aces grant agreement No 724427). This work has made use of data from the European Space Agency (ESA) mission *Gaia* (<https://www.cosmos.esa.int/gaia>), processed by the *Gaia* Data Processing and Analysis Consortium (DPAC, <https://www.cosmos.esa.int/web/gaia/dpac/consortium>). Funding for the DPAC has been provided by national institutions, in particular the institutions participating in the *Gaia* Multilateral Agreement.

References

Allart, R., Pino, L., Lovis, C., et al. 2020, arXiv:2010.15143
 Astudillo-Defru, N., & Rojo, P. 2013, A&A, 557, A56
 Astudillo-Defru, N., Delfosse, X., Bonfils, X., et al. 2017, A&A, 600, A13
 Ben-Yami, M., Madhusudhan, N., Cabot, S. H. C., et al. 2020, ApJ, 897, L5
 Borsa, F., Scandariato, G., Rainer, M., et al. 2015, A&A, 578, A64
 Borsa, F., & Zannoni, A. 2018, A&A, 617, A134
 Borsa, F., Rainer, M., Bonomo, A. S., et al. 2019, A&A, 631, A34
 Bourrier, V., & des Etangs, A. L. 2018, Handbook of Exoplanets, 148
 Bourrier, V., Kitzmann, D., Kuntzer, T., et al. 2020, A&A, 637, A36
 Bourrier, V., Ehrenreich, D., Lendl, M., et al. 2020, A&A, 635, A205
 Bouvier, J. 2008, A&A, 489, L53
 Brogi, M., de Kok, R. J., Albrecht, S., et al. 2016, ApJ, 817, 106
 Brogi, M., Line, M., Bean, J., et al. 2017, ApJ, 839, L2
 Brown, D. J. A., Triaud, A. H. M. J., Doyle, A. P., et al. 2017, MNRAS, 464, 810
 Cabot, S. H. C., Madhusudhan, N., Welbanks, L., et al. 2020, MNRAS, 494, 363
 Casasayas-Barris, N., Pallé, E., Nowak, G., et al. 2017, A&A, 608, A135
 Casasayas-Barris, N., Pallé, E., Yan, F., et al. 2019, A&A, 628, A9
 Casasayas-Barris, N., Pallé, E., Yan, F., et al. 2020, A&A, 635, A206

Chen, G., Pallé, E., Welbanks, L., et al. 2018, A&A, 616, A145
 Chen, G., Casasayas-Barris, N., Pallé, E., et al. 2020, A&A, 635, A171
 Delrez, L., Santerne, A., Almenara, J.-M., et al. 2016, MNRAS, 458, 4025
 Deming, L. D., & Seager, S. 2017, Journal of Geophysical Research (Planets), 122, 53
 Di Gloria, E., Snellen, I. A. G., & Albrecht, S. 2015, A&A, 580, A84
 Dravins, D., Lindegren, L., & Torkelsson, U. 1990, A&A, 237, 137
 Dreizler, S., Reiners, A., Homeier, D., et al. 2009, A&A, 499, 615
 Eastman, J., Gaudi, B. S. & Agol, E. 2013, PASP, 125, 923
 Ehrenreich, D., Lovis, C., Allart, R., et al. 2020, Nature, 580, 597
 Evans, T. M., Sing, D. K., Kataria, T., et al. 2017, Nature, 548, 58
 Evans, T. M., Sing, D. K., Goyal, J. M., et al. 2018, AJ, 156, 283
 Faria, J. P., Adibekyan, V., Amazo-Gómez, E. M., et al. 2020, A&A, 635, A13
 Fossati, L., Haswell, C. A., Froning, C. S., et al. 2010, ApJ, 714, L222
 Gaia Collaboration 2018, VizieR Online Data Catalog, I/345
 Gibson, N. P., Merritt, S., Nugroho, S. K., et al. 2020, MNRAS, 493, 2215
 Gustafsson, B., Edvardsson, B., Eriksson, K., et al. 2008, A&A, 486, 951
 Hoeijmakers, H. J., Ehrenreich, D., Heng, K., et al. 2018, Nature, 560, 453
 Hoeijmakers, H. J., Ehrenreich, D., Kitzmann, D., et al. 2019, A&A, 627, A165
 Hoeijmakers, H. J., Seidel, J. V., Pino, L., et al. 2020, A&A, 641, A123
 Israelian, G., Delgado Mena, E., Santos, N. C., et al. 2009, Nature, 462, 189
 Kovács, G., & Kovács, T. 2019, A&A, 625, A80
 Lothringer, J. D., Barman, T., & Koskinen, T. 2018, ApJ, 866, 27
 McLaughlin, D. B. 1924, ApJ, 60, 22
 Merritt, S. R., Gibson, N. P., Nugroho, S. K., et al. 2020, A&A, 636, A117
 Mikal-Evans, T., Sing, D. K., Goyal, J. M., et al. 2019, MNRAS, 488, 2222
 Mollière, P., Wardenier, J. P., van Boekel, R., et al. 2019, A&A, 627, A67
 Noyes, R. W., Hartmann, L. W., Baliunas, S. L., et al. 1984, ApJ, 279, 763
 Ohta, Y., Taruya, A., & Suto, Y. 2005, ApJ, 622, 1118
 Oshagh, M., Triaud, A. H. M. J., Burdanov, A., et al. 2018, A&A, 619, A150
 Parmentier, V., Line, M. R., Bean, J. L., et al. 2018, A&A, 617, A110
 Pepe, F. A., Cristiani, S., Rebolo Lopez, R., et al. 2010, Proc. SPIE, 77350F
 Pepe, F., Molaro, P., Cristiani, S., et al. 2014, Astronomische Nachrichten, 335, 8
 Pepe, F., Cristiani, S., Rebolo, R., et al. 2020, arXiv:2010.00316
 Piskunov, N., & Valenti, J. A. 2017, A&A, 597, A16
 Plez, B. 2012, Turbospectrum: Code for spectral synthesis, ascl:1205.004
 Reiners, A., & Schmitt, J. H. M. M. 2002, A&A, 384, 155
 Reiners, A., Schmitt, J. H. M. M., 2003, A&A, 398, 647
 Rossiter, R. A. 1924, ApJ, 60, 15
 Ryabchikova, T., Piskunov, N., Kurucz, R. L., et al. 2015, Phys. Scr, 90, 054005
 Salz, M., Schneider, P. C., Fossati, L., et al. 2019, A&A, 623, A57
 Seager, S., & Mallén-Ornelas, G. 2003, ApJ, 585, 1038
 Serrano, L. M., Oshagh, M., Cegla, H. M., et al. 2020, MNRAS, 493, 5928
 Sing, D. K., Lavvas, P., Ballester, G. E., et al. 2019, AJ, 158, 91
 Snellen, I. A. G. 2004, MNRAS, 353, L1
 Snellen, I. A. G., Albrecht, S., de Mooij, E. J. W., & Le Poole, R. S. 2008, A&A, 487, 357
 Snellen, I. A. G., de Kok, R. J., de Mooij, E. J. W., et al. 2010, Nature, 465, 1049
 Stangret, M., Casasayas-Barris, N., Pallé, E., et al. 2020, A&A, 638, A26
 Tabernero, H. M., Dorda, R., Negueruela, I., et al. 2018, MNRAS, 476, 3106
 Tabernero, H. M., Marfil, E., Montes, D., et al. 2019, A&A, 628, A131
 Tabernero, H., et al. 2020, A&A, submitted
 Ter Braak, C. J. F. 2006, Statistics and Computing, 16, 239
 Vidal-Madjar, A., Lecavelier des Etangs, A., Désert, J.-M., et al. 2003, Nature, 422, 143
 Vidal-Madjar, A., Lecavelier des Etangs, A., Désert, J.-M., et al. 2008, ApJ, 676, L57
 Vidal-Madjar, A., Arnold, L., Ehrenreich, D., et al. 2010, A&A, 523, A57
 Winn, J. N., Johnson, J. A., Narita, N., et al. 2008, ApJ, 682, 1283
 Wytenbach, A., Ehrenreich, D., Lovis, C., et al. 2015, A&A, 577, A62
 Yan, F., Pallé, E., Fosbury, R. A. E., et al. 2017, A&A, 603, A73
 Yan, F., & Henning, T. 2018, Nature Astronomy, 2, 714
 Yan, F., Casasayas-Barris, N., Molaverdikhani, K., et al. 2019, A&A, 632, A69

-
- ¹ INAF – Osservatorio Astronomico di Brera, Via E. Bianchi 46, 23807 Merate (LC), Italy
 - ² Département d’astronomie, Université de Genève, ch. des Maillettes 51, 1290 Versoix, Switzerland
 - ³ INAF – Osservatorio Astrofisico di Torino, Via Osservatorio 20, I-10025 Pino Torinese, Italy
 - ⁴ Fundación G. Galilei - INAF (TNG), Rambla J. A. Fernández Pérez 7, E-38712 Breña Baja (La Palma), Spain
 - ⁵ INAF – Osservatorio Astronomico di Trieste, via Tiepolo 11, 34143 Trieste, Italy
 - ⁶ Instituto de Astrofísica de Canarias, C/Vía Láctea s/n, E-38205 La Laguna (Tenerife), Spain
 - ⁷ Universidad de La Laguna (ULL), Departamento de Astrofísica, 38206 La Laguna, Tenerife, Spain
 - ⁸ Centro de Astrobiología (CSIC-INTA), Carretera de Ajalvir km 4 - 28850 Torrejón de Ardoz, Madrid, Spain
 - ⁹ INAF – Osservatorio Astronomico di Palermo, Piazza del Parlamento, 1, 90134, Palermo, Italy
 - ¹⁰ Instituto de Astrofísica e Ciências do Espaço, Universidade do Porto, CAUP, Rua das Estrelas, 4150-762 Porto, Portugal
 - ¹¹ Departamento de Física e Astronomia, Faculdade de Ciências, Universidade do Porto, Rua do Campo Alegre, 4169-007 Porto, Portugal
 - ¹² Centro de Astrofísica da Universidade do Porto, Rua das Estrelas, 4150-762 Porto, Portugal
 - ¹³ European Southern Observatory, Karl-Schwarzschild-Strasse 2, 85748 Garching b. Munchen, Germany
 - ¹⁴ Universitat Bern, Physikalisches Institut, Siedlerstrasse 5, 3012 Bern, Switzerland
 - ¹⁵ Faculdade de Ciências da Universidade de Lisboa (Departamento de Física), Edifício C8, 1749-016 Lisboa, Portugal
 - ¹⁶ Instituto de Astrofísica e Ciências do Espaço, Universidade de Lisboa, Edifício C8, 1749-016 Lisboa, Portugal
 - ¹⁷ Consejo Superior de Investigaciones Científicas, E-28006 Madrid, Spain
 - ¹⁸ ESO, European Southern Observatory, Alonso de Cordova 3107, Vitacura, Santiago
 - ¹⁹ Institute for Fundamental Physics of the Universe, IFPU, Via Beirut 2, 34151 Grignano, Trieste, Italy